

RSC Advances



This is an *Accepted Manuscript*, which has been through the Royal Society of Chemistry peer review process and has been accepted for publication.

Accepted Manuscripts are published online shortly after acceptance, before technical editing, formatting and proof reading. Using this free service, authors can make their results available to the community, in citable form, before we publish the edited article. This *Accepted Manuscript* will be replaced by the edited, formatted and paginated article as soon as this is available.

You can find more information about *Accepted Manuscripts* in the [Information for Authors](#).

Please note that technical editing may introduce minor changes to the text and/or graphics, which may alter content. The journal's standard [Terms & Conditions](#) and the [Ethical guidelines](#) still apply. In no event shall the Royal Society of Chemistry be held responsible for any errors or omissions in this *Accepted Manuscript* or any consequences arising from the use of any information it contains.

Soy Polyester Urethane/TiO₂ and Ce-TiO₂ Nanocomposites: Preparation, Characterization and Evaluation of Electrochemical Corrosion Resistance Performance

Names of Authors

First Author

Obaid ur Rahman

Research scholar

Materials Research Laboratory, Department of Chemistry

Jamia Millia Islamia, New Delhi. 110025.

Email: obbi16@gmail.com

***Corresponding Author**

Dr. Sharif Ahmad

Professor

Materials Research Laboratory, Department of Chemistry

Jamia Millia Islamia, New Delhi. 110025

Email: sharifahmad_jmi@yahoo.co.in

Tel no. +91 11 26827508

Fax: +91 11 26840229

Soy Polyester Urethane/TiO₂ and Ce-TiO₂ Nanocomposites: Preparation, Characterization and Evaluation of Electrochemical Corrosion Resistance Performance

Obaid ur Rahman and Sharif Ahmad*

Materials Research Laboratory, Department of Chemistry, Jamia Millia Islamia,
New Delhi-110025, India

ABSTRACT

Environment friendly soy polyester urethane nanocomposite coating materials were prepared by dispersing the TiO₂ and Ce-TiO₂ nanoparticles in 3-Isocyanatopropyltriethoxysilane (IPTES) modified soy oil (SO) polyester urethane triethoxysilane (PEUTES) matrix *via* sonication technique. Fourier Transform Infrared Spectroscopy (FT-IR), ¹H and ¹³C Nuclear Magnetic Resonance (NMR) Spectroscopy, Scanning Electron Microscopy (SEM), Energy-Dispersive X-Ray Spectroscopy (EDX), X-ray Diffraction (XRD), Transmission Electron Microscope (TEM), UV-Visible Spectroscopy (UV) were employed to characterize the synthesized coating materials. The anticorrosion ability of nanocomposites and that of PEUTES coatings on carbon steel (CS) in 3.5 wt. % NaCl solution was investigated using Potentiodynamic Polarization (PDP), Electrochemical Impedance Spectroscopy (EIS) techniques and salt mist test. The effects of dispersion of nano TiO₂ and Ce-TiO₂ fillers in PEUTES matrix on hydrophobic, physico-mechanical, thermal and anticorrosive properties was also studied. The TiO₂ and Ce-TiO₂ nanofiller dispersed soy polyester urethane nanocomposite coatings have exhibited far superior corrosion resistance properties than those of other such reported systems. These studies revealed the presence of nanofiller in polyester urethane matrix, induces strong barrier and locking effect at the coating-metal interface. The higher impedance value ($\approx 108 \Omega$) and lower corrosion rate (7.8518×10^{-6} mpy) confirm the superior protection ability of nanocomposite.

Keywords: Titanium oxide, Ce doped Titanium oxide, nanoparticles, Nanocomposites, Corrosion, Polyester urethanes and electrochemical impedance spectroscopy.

1. INTRODUCTION

Metallic corrosion causes catastrophic losses in terms of deterioration of devices, machines, industrial setups, infrastructures and economy.¹ Various protective techniques are being used to save such losses there by enhancing their service life.² Among these protective techniques, the formulation and application of polymer coatings on the substrate is easy and more convenient.³ The presence of various pendent functional groups in polymer coatings significantly improve the adhesion at coating metal interfaces, which enhances the physico-mechanical and anticorrosive properties of coatings.⁴ However, the use of organic solvents in polymer coating systems produces volatile organic contents (VOCs), which lead to the number of harmful effects on the environment.³ Moreover, the depletion of fossil fuel reservoir has forced the scientists and technologists to develop sustainable resource based polymers. Among various sustainable precursors, vegetable oils (VOs)⁵ are readily available, which are biodegradable, inexpensive and containing numerous functional groups (ester, double bonds, hydroxyl etc.) accessible to chemical transformation. Generally, VO polymers have excellent chemical, physical, hydrophobic,⁶ and good fluid properties owing to their low molecular weight.⁵ Nevertheless they exhibit low rigidity, poor mechanical strength, unsatisfactory acid and base resistance properties, which limit their application under stringent environmental conditions.³ In order to enhance the useful properties and to overcome the drawbacks of sustainable polymers, new approaches are being adopted. The dispersion of nanofillers in VO polymers is one of them, which leads to the formation of new generation polymeric materials exhibiting excellent mechanical, thermal and barrier properties.^{7,8}

Titanium oxide (TiO₂) and Ce doped TiO₂ are considered as the most versatile and technologically important materials, having promising applications in the field of electronics, catalysis and pigments. The presence of higher number of electron-hole pairs in Ce increases the redox potential of Ce doped nano TiO₂ particles which enhances the anticorrosive activity of Ce-TiO₂ fillers.⁹ Electronic, photoelectric, catalytic and anticorrosive properties of nano TiO₂

and Ce doped TiO₂ have previously been reported.⁹ However, their synthesis in presence of castor oil using titanium tetra isopropoxide and cerium ammonium nitrate has not been reported so far.

The present article reports, for the first time, the synthesis of TiO₂ and Ce doped TiO₂ using castor oil (a sustainable resource) has been reported for the first time. The structural, morphological and thermal stability of these coatings were investigated using different analytical techniques. The effect of presence of TiO₂ and Ce-TiO₂ nanoparticles in PEUTES coatings on thermal stability, hydrophobicity, physico-mechanical and anticorrosive properties were also investigated. These studies revealed that the nanocomposite coatings have exhibited far superior properties than those of other such reported systems.

2. EXPERIMENTAL

2.1. Materials

Titanium tetra-isopropoxide (TTIP) 97% was purchased from High Media Laboratories Pvt. Ltd. Mumbai, India. Acetic acid (99.7%), cerium ammonium nitrate (CAN), castor oil, sodium hydroxide, sulphuric acid, ethanol dimethylolpropionic acid (DMPA), 50% hydrogen peroxide, glacial acetic acid (99-100%), were obtained from sd Fine-Chemicals Limited, Mumbai, India. Soy oil (SO) was procured from the Kendriya Bhandar, Jamia Millia Islamia, New Delhi, India, while dibutyl tin dilaurate (DBTDL) and 3-isocyanatopropyltriethoxysilane (IPTES) were supplied by Alfa Aesar, UK. All the chemicals were of AR grades and used as such.

2.2. Preparation of soy polyester and IPTES based polyester urethane (PEUTES) hybrid

The fatty acid polyester (FPE) was synthesised by extracting the fatty acid (FA) from soy oil (supporting information),¹⁰ followed by its epoxidation and hydroxylation, which lead to the formation of soy fatty acid polyol (FPOL).¹¹ The FPOL and DMPA were mixed in 1:4 ratio along with 1-2 drops of 1 wt. % aqueous solution of p-Toluenesulphonic acid (PTSA) were

used as acid catalyst under continuous stirring at 120 °C followed by condensation reaction between the hydroxyl groups of FPOL and carboxyl groups of DMPA through the elimination of water resulted in the formation of crosslinked three dimensional fatty acid polyester (FPE) after 2 h as per (Scheme 1 a).¹² The progress of the reaction was monitored by acid value and FTIR spectra taken at regular intervals of time. Further, FPE and IPTES were mixed in 4:1 ratio by weight, allowed to react then in presence of dibutyltindilaurate (DBTDL) catalyst. The reaction mixture continuously stirred on a magnetic stirrer at 60 °C for 30 min which led to the formation of highly crosslinked hybrid nano silica networked polyester urethane (PEUTES) coating material. The progress of these reactions was periodically monitored by FT-IR spectra. The disappearance of >NCO peak at 2276 cm⁻¹ confirmed the formation of PEUTES hybrid material.¹³

2.3. Synthesis of TiO₂ and Ce-TiO₂ Nanoparticles

TTIP (25 ml) was drop wise added to the mixture of acetic acid (48 ml) and castor oil (100 ml), in a 250 mL three necked flat bottom flask fitted with condenser, thermometer and magnetic stirrer, then 50 mL distilled water was slowly added to the reaction mixture under vigorous stirring at room temperature (≈30 °C), the reaction mixture was continuously stirred overnight at room temperature to get a transparent sol, which was further heated at 100 °C for 1 h, followed by its calcination at 600 °C in air for 4 h, which resulted in the formation of TiO₂, the same was doped with the Ce, which was used for the synthesis of Ce-TiO₂-I and Ce-TiO₂-II nanoparticles, respectively. The preparation of Ce-TiO₂ nanoparticles in two different ratios (TTIP: CAN in 3:1 and 1:1 molar ratio) was carried out using the same procedure and reaction setup that was used for the preparation of TiO₂ nanoparticles. The formation of nano TiO₂ and Ce-TiO₂ was confirmed by XRD and FTIR studies.

2.4. Preparation of PEUTES-TiO₂ and PEUTES-Ce-TiO₂ hybrid nanocomposites

The 1.5 wt. % of TiO₂, Ce-TiO₂-I and Ce-TiO₂-II nanoparticles were dispersed in PEUTES ultrasonically using minimum amount of ethanol (solvent) and sonicated for 1 h to obtain the

homogeneously dispersed nanoparticle suspended colloidal solutions of PEUTES-TiO₂, PEUTES-Ce-TiO₂-I and PEUTES-Ce-TiO₂-II nanocomposites.

2.5. Preparation and testing of coatings

The carbon steel (CS) strips (composition: 2.87 wt. % C and 97.13 wt. % Fe)³ of two different sizes were polished with different grades of silicon carbide papers (180, 320 and 500) followed by thorough rinsing with water and degreased with alcohol and acetone. PEUTES, PEUTES-TiO₂, PEUTES-Ce-TiO₂-I and PEUTES-Ce-TiO₂-II nanocomposites were applied on the surfaces of the CS strips by brush techniques and were kept at room temperature for drying. The coatings of ≈ 120 μm thickness developed on CS of size 70 mm \times 25 mm \times 1 mm were used for the physicomechanical studies and that of 25 mm \times 25 mm \times 1 mm size were used for electrochemical corrosion and morphological studies.

2.6. Instrumentation

Different analytical techniques were used to characterize the nanoparticles and nanocomposite coating materials. Powder X-ray diffraction (XRD) patterns were obtained by a Rigaku Mini Flex diffractometer (using Cu K λ = 1.5418 Å radiation) at a scanning rate of 0.002° per min in the 20° to 70° range. Fourier transform infrared (FT-IR) spectra were recorded on IR Affinity-1 Shimadzu, (in the range of 4000 to 400 cm⁻¹). The ¹H and ¹³C NMR spectra of the PEUTES were obtained on a JEOL GSX 300 MHz FX-100 in CDCl₃ using tetramethylsilane (TMS) as internal standard. UV-visible spectra were recorded in aqueous medium on Perkin Elmer Lambda Spectrophotometer (Model EZ-221). The transmission electron microscopy (TEM) and selected area electron diffraction (SAED) patterns of the samples were recorded using a JEOL-2100 TEM instrument, operating at 200 kV. Scanning electron microscopy (SEM) and energy dispersive X-ray spectroscopy (EDX) examinations were carried out on Zeiss EVO 40 instrument at the Advanced Instrumentation Research Facility (AIRF), Jawaharlal Nehru University, New Delhi.

The dry to touch (DTH) and dry to hard time (DTT) of coatings were recorded, the scratch hardness (SH) [BS 3900], impact resistance (IR) [IS; 101 part 5/sec-3, 1998], bending test (BT) [ASTM-D3281- 84] were performed, while specular gloss (at 45°) and thicknesses of coatings were measured by Gloss meter (Model-RSPT-20) and Elcometer (Model 345; Elcometer Instrument, Manchester, UK), respectively. The cross-hatch test (ASTM D3359) was carried out on coated CS by cross hatch meter.¹⁴ The thermal stabilities of coating materials were studied by thermogravimetric analysis (TGA) using EXSTAR TG/DTA 6000 instrument under nitrogen atmosphere at a heating rate of 10 °C min⁻¹ from 25-800 °C. The glass transition temperatures (T_g) of coating materials were determined by differential scanning calorimetry (DSC) (SII EXSTAR 6000, DSC620, Japan) the heating and cooling of the samples were performed at the rates of 10 °C min⁻¹ under nitrogen atmosphere in the temperature range of 25-200 °C. The contact angle measurements for the hydrophobicity of coatings were evaluated by dropping the deionized water using a Drop Shape Analysis System (model DSA10MK2, Kruss GmbH, Germany) image captured with the help of an attached high speed CCD camera. The contact angles of these coatings were found in the range of 87°-95°.¹⁵ Ultrasonic wave sonicator (model No. 1.5L, 50Hz) was used at 30 °C for the homogeneous dispersion of nanoparticles in the polymeric matrix.

The corrosion resistance performance of PEUTES, PEUTES-TiO₂, PEUTES-Ce-TiO₂-I and PEUTES-Ce-TiO₂-II nanocomposite coated and uncoated CS were carried out on Potentiostat/Galvanostat microAutolab type III (μ 3AVT 70762, The Netherland) in 3.5 wt. % NaCl, at 30 °C according to ASTM G 59-97 standard using EG & G flat cell of 400 mL capacity consisting of conventional three electrodes, i.e. 1.0 cm² area of coated and uncoated CS as working electrode exposed to the corrosive medium, Pt gauge as auxiliary electrode and Ag/AgCl as reference electrode were used for corrosion studies. The electrochemical setup was supported by software Nova 1.8 (Autolab,UK); enabling the study of electrochemical corrosion behavior of coated and uncoated CS. The impedance and Tafel

parameters were obtained by curve fitting procedure available in the software. After stabilizing the equipment for 30 min, the electrochemical corrosion behavior of coated and uncoated CS was taken with reference to their respective open circuit potentials (OCP). The AC (alternating-current) impedance measurements were made at open circuit potentials with 20 mV amplitude of the sinusoidal voltage signal at applied frequencies in the range of 100 KHz to 0.1 Hz using ten points per decade. The polarization curves were recorded by sweeping the potential from -100 mV to $+100$ mV (with respect to OCP) in the noble direction at a constant scan rate of 0.001 mV/s. The working electrodes were kept in the test solutions for 30 min to stabilize the electrode and to ensure that no blistering occurs during the incubation period before the impedance run. The impedance spectra obtained for the PEUTES, PEUTES-TiO₂, PEUTES-Ce-TiO₂-I and PEUTES-Ce-TiO₂-II coated CS and uncoated CS can be used to model the electrochemical corrosion behavior of coated substrate by an equivalent circuit and were found to be reproducible upto $\pm 2-3\%$. The equivalent electrical circuit (EEC) is often used to analyze (Supplementary figure 1, supporting information) the impedance spectra of a metal/coating system and $R_s (C_c (R_{po} (C_{dl} R_{ct})))$ circuit model to simulate the changes in the properties of the coatings, where, R_s is the solution resistance, R_{po} is the pore resistance, R_{ct} is the coating resistance while the C_c and C_{dl} are the constant phase element and the double layer capacitance of the coating respectively. The EEC consists of two time constants; the first time constant ($R_{po}C_c$) in the high frequency region, attributed to the intrinsic properties of the coating and the second time constant ($C_{dl}R_{ct}$) in low frequency region, attributed to the corrosion reaction at coating-metal interface. These coatings were exposed to 3.5 wt. % NaCl solution for EIS studies for 144 h. The Polarization resistance (R_p) of test samples was evaluated using the slope of the potential-current plot (Tafel plots), according to the Stern-Geary equation:¹⁶

$$R_p = \frac{b_a b_c}{2.303(b_a + b_c)I_{corr}} \quad (1)$$

Here I_{corr} is the corrosion current density, determined by an intersection of the linear portions of the anodic and cathodic curves, while b_a and b_c are anodic and cathodic Tafel slopes ($\Delta E/\Delta \log I$), respectively.

Salt mist test (ASTM B 117-94) for PEUTES-TiO₂, PEUTS-Ce-TiO₂-I and PEUTES-Ce-TiO₂-II nanocomposites coated CS specimen was carried out for a period of 480 h in the salt mist chamber under 5.0 wt. % NaCl solution at 90% humidity.

3. RESULTS AND DISCUSSION

3.1. Synthesis

A sustainable approach was applied to synthesised PEUTES matrix using SO as sustainable precursor, FA was extracted from SO to obviate the effect of steric hindrance,⁶ followed by epoxidation and trans-hydroxylation for the synthesis of FPOL.¹¹ During the formation of FPE number of hydroxyl groups further increases and by the reaction of carboxylic and hydroxyl functionalities of DMPA with FPOL and vice versa (Scheme 1b). The unreacted hydroxyl groups were allowed to react with isocyanate group of IPTES in the presence of DBTDL catalyst to form organic-inorganic hybrid PEUTES matrix (Scheme 1b).

The TiO₂ and Ce-TiO₂ nanoparticles were prepared in castor oil *via* sol-gel technique using TTIP and CAN. The castor oil acts as a nontoxic and multi-functional reagent, acting as a medium stabilizing and dispersing agents for nanoparticles synthesis.¹⁷ Crystal lattice formed by TiO₂ nanoparticles and Ce atoms are aligned within the crystal lattice at the grain boundaries site of the TiO₂ crystals. On the other hand, due to higher ionic size of Ce ions, Ti ions may enter into the Ce lattice leading to the formation of the mixed phase of Ce_xTiO₂ nanoparticles.¹⁸ Furthermore, TiO₂ and Ce-TiO₂ nanoparticles homogenously dispersed in PEUTES hybrids to form the nanocomposite coating material through sonication.

3.2. X-ray diffraction (XRD) studies

The XRD spectra of TiO₂ and Ce-TiO₂ as shown in Figure 1(a-c). The characteristic diffraction peaks are present at $\theta = 25.3^\circ, 37.8, 48.1, 62.8$ etc. of TiO₂ (Figure 1a) indexed to the pure anatase phase of TiO₂ (JPCDS No. 89-4921) as reported in the literature.¹⁹ Ce-TiO₂ was transformed to different phase, depending on the oxidation state of cerium. As we know that the ionic radii of Ce⁺³ ion is greater than Ti⁺⁴. SO, the cerium ion could not doped in Ti⁺⁴ lattice, however, cerium ion can fit into the TiO₂ crystal lattice along the grain sides. While due to shorter ionic radii, Ti⁺⁴ will dope inside Ce⁺³ lattice in either case Ce and Ti combine with each other, which leads to the formation of a mixed phase as per Figure 1.¹⁸ The presence of Ce⁺³ ions in Ce-TiO₂ nanoparticles induces formation of mixed phases such as Ce₂TiO₅, Ce₂Ti₂O₇ and Ce₄Ti₉O₂₄, while CeTiO₄ and CeTi₂O₆, contain Ce⁴⁺ ions.²⁰ XRD analysis of mixed oxides of Ce and Ti indicated that the doping of cerium in TiO₂, (JPCDS No. 49-1606) is an orthorhombic structural system with primitive lattice. According to the diffraction angle of new peak ($\theta = 28.5^\circ$), it can be indexed to CeO₂ phase, suggesting that a significant portion of Ce³⁺ ions were oxidized into Ce⁴⁺ during sintering.¹⁸ The average crystalline size of all these samples were analyzed with the help of lower full-width-at-half-maximum (FWHM) of the anatase (101) diffraction peak and found in accordance with the reported literature using Scherrer's equation.²¹

$$D = \frac{0.9\lambda}{\beta \cos\theta} \quad (2)$$

where D is the particle size, λ is the X-ray wavelength (nm), θ is Bragg's angle; β is the excess line broadening (radian), and the particle size of nanoparticles was found to be 25, 15 and 10 nm for TiO₂, Ce-TiO₂-I and Ce-TiO₂-II, respectively.

3.5. UV-Visible spectroscopic studies

Figure 2 shows The UV absorption spectra of TiO₂, Ce-TiO₂-I and Ce-TiO₂-II with the maximum absorption in the UV region. The peak at ≈ 325 nm increase of Ce-TiO₂ shifted

slightly towards the visible region (at ≈ 340 nm) due to the doping of Ce in TiO₂ matrix.²² Furthermore, the increase in the intensity of peak is also observed with the increased loading of Ce. The synthesized Ce-TiO₂-I and Ce-TiO₂-II were annealed in atmospheric air at 600 °C, resulting in the oxidation of cerium leading to the formation of CeO₂ and Ce₂O₃, respectively.²⁰ The peak broadening was observed in the absorbance spectra of Ce-TiO₂-I and Ce-TiO₂-II at 340 nm which can be assigned to the f-d transition of single electron from 4f to 5d subshells of Ce³⁺ ions, as Ce⁴⁺ ion does not contain any electron in its ground state (4f⁰ 5d⁰).²³ Hence, the UV spectral analysis revealed that the (+3) valence state is predominantly present in the matrix of the TiO₂ nanoparticles.²⁴

3.4. FT-IR spectroscopic studies

The peaks at 2910 and 2854 cm⁻¹ are assigned to the C–H stretching vibration of the aliphatic chain present in the SO (Figure 3). Besides, the peak at 3009 cm⁻¹ assigned to the –C=C–H stretching vibration present in soy oil FA chain (Figure 3a), which get disappeared in FPOL and a new peak was observed at 3490 cm⁻¹ in the FT-IR spectrum (Figure 3b). These results confirmed the conversion of double bonds of FA chain into hydroxyl groups via epoxidation and trans hydroxylation. The appearance of absorption band at 1700 cm⁻¹ in FPE (Figure 3c) revealed that the hydroxyl groups of FPOL had reacted with carboxyl functionality of DMPA.¹¹ Some new changes were observed in the FT-IR the spectrum of PEUTES as compared to that of FPE, such as the characteristic vibration peak of NCO group at 2276 cm⁻¹ disappeared in the spectrum of PEUTES (Figure 3d), revealing that the hydroxyl functionality of FPE had reacted with the isocyanate groups of IPTES.²⁵ Apart from this peak, a new peak appeared at 1544 cm⁻¹ during the course of the reaction, which corresponds to the bending vibrations of the amide linkages of urethane.²⁶ The appearance of an additional strong absorption band in the range 1074-1120 cm⁻¹ due to asymmetric vibration modes of the Si-O-Si bonds confirms the *in situ* formation of silica nanoparticles in the FPE matrix.²⁴

The peak at 471 cm^{-1} and at 425 cm^{-1} (Figure 4) can be attributed to Ti–O–Ti as well as Ti–O–Ce vibrations, respectively. Thus, the shift in peak by 46 cm^{-1} from 471 cm^{-1} to 425 cm^{-1} as observed in Ce-TiO₂-I, while the peak shift from to 410 cm^{-1} in Ce-TiO₂-II, confirms the formation of Ti–O–Ce bonds.²⁷

3.6. ¹H-NMR and ¹³C-NMR analysis

In ¹H NMR spectrum of PEUTES (Figure 5), the peak at $\delta=0.94$ ppm can be attributed to the terminal methyl groups of the fatty acid chains, and the signal at $\delta=1.02$ – 1.20 ppm corresponds to the –CH₂ groups attached to the terminal methyl group and CH₂ groups of the fatty acid chains.²⁸ The peak at $\delta=4.17$ ppm is assigned to –OH groups, the characteristic peaks for –CH₂–O–CO also appeared in the same region at $\delta=3.8$ – 3.9 ppm.²⁹ The chemical shift value at $\delta=5.0$ – 5.9 ppm can be assigned to the hydrogen of urethane linkages³⁰ while the peak at $\delta=4.72$ ppm is due to the methylene protons attached to oxygen linking the urethane functional groups (–CH₂–O–CO–NH–).³¹ The ¹³C NMR spectrum (Supplementary figure 3, supporting information) of PEUTES shows the peak at $\delta=174$ – 178 ppm corresponding to the carbonyl carbon of ester linkages. The peak in the region of $\delta=30$ – 70 ppm is assigned to the carbon atom directly attached to an oxygen atom while the peak at $\delta=34.5$ ppm corresponds to the tertiary carbon atoms of DMPA.³² Further, the presence of peak at $\delta=66.2$ ppm (–CH₂–O–Si–) confirmed the inclusion of IPTES in polymer matrix.³³

3.7. Morphological Studies

(i) Transmission electron microscopy (TEM) analysis

The TEM images of TiO₂, Ce-TiO₂-I, Ce-TiO₂-II (Figure 6a-c) revealed the changes in morphologies with the corresponding changes in the average particle size. A cubic morphology was observed in case of the TiO₂ having 10–15 nm particle size whereas the

Ce-TiO₂-I exhibits spherical morphology with the particle size of 5-10 nm range, while a mix cubic and spherical morphologies were seen for Ce-TiO₂-II in the 10-15 nm particle size range. Furthermore, the average particle size obtained from the TEM measurements are well in agreement with those obtained from the XRD measurements. The HR-TEMs (Figure 6 d-f) of TiO₂, Ce-TiO₂-I and Ce-TiO₂-II exhibit crystalline lattices for TiO₂, Ce-TiO₂-I, Ce-TiO₂-II respectively, confirming the anatase and rutile (phase) types of the crystal structures given in section 3.2. TEM micrographs of PEUTES, PEUTES-TiO₂, PEUTES-Ce-TiO₂-I and PEUTES-Ce-TiO₂-II are given in Supplementary figure 4a-c. In these micrographs (Supplementary figure 4a), homogeneously dispersed silica nanoparticles formed *in situ* are clearly visible while the Supplementary figure 4b-d show the TiO₂, Ce-TiO₂-I and Ce-TiO₂-II dispersion in nanocomposite coatings, which is encapsulated by the polymeric matrix.³⁴

(ii) Scanning electron microscopy (SEM) studies

The SEM micrographs (Figure 7a-c) of TiO₂ (a), Ce-TiO₂-I (b) and Ce-TiO₂-II (c) show that the TiO₂, Ce-TiO₂-I and Ce-TiO₂-II consist of well-defined cubical and nanoparticles with an average dimension of less than 15 nm as discussed in previous section 3.7 (i). The EDX spectra (Supplementary Figure 2 a-c) of TiO₂, Ce-TiO₂-I and Ce-TiO₂-II nanoparticles show the composition of their constituents in wt% clearly reveals that the increase in the Ce content in Ce-TiO₂ with the increased loading of CAN in the reaction mixture. The SEM micrographs of PEUTES coated CS (Figure 7d-e) indicate a cross-linked structure with O-Si-O- acting as a bridging moiety in PEUTES (Figure 7d-e).

3.8. Thermal Behavior

Figure 8 and 9 show thermal behavior of organic-inorganic hybrid and nanocomposite coatings. These coatings show 5.0 wt. % loss around 185 °C due to the desorption of physically adsorbed solvent and reacted moieties. The decomposition of labile urethane groups occurred at temperature 285 °C showing 18 wt. % loss.³⁵ In the temperature range

350-390 °C, 51 wt. % loss was observed due to the degradation of ester moieties present in the coating matrix.³⁶ While the 70 wt.% loss at around 465 °C occurred due to the partial decomposition of the silicone entrapped polymeric segments.³⁷ Nanocomposite coatings showed the same degradations pattern, but at higher temperatures i.e, 5 wt. % at 220 °C, 20 wt. % at 320 °C and 70 wt. % loss at 590-660 °C. The improved thermal stability of nanocomposites coatings can be explained by an increase in physical interaction of TiO₂ and Ce-TiO₂ with the polymer matrix.

The glass transition temperature of PEUTES and nanocomposites were observed in the range of 110-160 °C (Figure 9). The increased T_g values in PEUTES and nanocomposite coatings of different composition attributed to the formation of highly cross linked structure and the filling of interstitial spaces of the matrix by nanoparticles.³⁸

3.10. Coating properties

(i) Physico-mechanical properties of PEUTES and nanocomposite coatings

The toughness of the synthesized nanocomposite coatings were evaluated by scratch hardness test (SHT). The increase in SHT value from PEUTES to PEUTES-TiO₂, PEUTES-Ce-TiO₂-I and PEUTES-Ce-TiO₂-II nanocomposite coatings, can be correlated to the increase in interfacial adhesion between the coating material and the CS substrate. The strong adhesion between coating material and substrate surface, which was further confirmed by cross hatch test. The optical micrographs of the sample before and after cross-cut test are shown in Supplementary Figure 5. The results are specified as a 5B class (Supplementary Table 1), representing an excellent adhesion between the nanocomposite coatings and CS substrate as no peeling was observed during the flaking step by tape. This can be attributed to the presence of polar functionalities such as -OH, -COOH; O-Si-O- linkages, TiO₂ and Ce-TiO₂ in hybrid polymer, which enhances the interfacial interactions with the substrate. All the coatings passed the 1/8 inch conical mandrel bend test and 26.8 kg/cm impact test summarized in Table S1 (given in supporting information). These results suggest that the presence of nanoparticles and pendant in the matrix are responsible for the flexibility of the coatings, thus coating can bend along with substrate without showing any sign of damage.

Further, the presence of O-Si-O, TiO₂ and Ce-TiO₂ in PEUTES has an impact on dissipation of energy during the impact test.

(ii) Potentiodynamic polarization (PDP) studies

Potentiodynamic polarization techniques were used to determine various electrochemical corrosion parameters like corrosion potential (E_{corr}), corrosion current density (I_{corr}) and corrosion rate to analyze instantaneous corrosion rate of coated specimens. Better corrosion protection was given by a coating showing lower corrosion rate, which corresponds to a lower I_{corr} or a higher E_{corr} values.³⁹ Figure 10 shows the PDP curves in saline medium, and the parameters are displayed in Table 1. Nanocomposite coatings showed an increase in E_{corr} values and decrease in I_{corr} values in comparison to PEUTES (-0.5327V) coatings and bare CS (-0.66951V) (Table 1). The superior corrosion resistance performance displayed by PEUTES with respect to bare CS is due to the presence of hydrolytically stable urethane bonds, flexible hydrocarbon chains, formation of *in situ* siloxane nanoparticles and good adhesion between PEUTES and CS substrate.

However, in case of nanocomposite coatings, dispersion of inorganic nano fillers in polymer matrix form strong barrier to the penetration of corrosive ions by providing the torturous path to the corrosive species to enter coating metal interface,⁴⁰ which was further confirmed by the low corrosion rate of nanocomposite coatings in comparison to that of PEUTES coatings (Table 1). The enhanced anticorrosive performance of PEUTES-TiO₂, PEUTES-Ce-TiO₂-I and PEUTES-Ce-TiO₂-II nanocomposite coated CS in comparison to PEUTES coated CS can be correlated to the inclusion of nano-fillers by filling the free volume and interstitial spaces present in the crosslinked network structure and increased adhesion between coating and metal surface.⁴⁰⁻⁴¹

Beyond 25% loading of Ce in Ce-TiO₂, causes significant reduction in corrosion inhibition ability which is reflected by a negative shift in corrosion potential and higher corrosion current density as well as higher corrosion rates that may be due to the formation of

Ce⁺³/Ce⁺⁴ redox couple,⁹ the PDP study revealed that PEUTES-Ce-TiO₂-I showed best corrosion protection among different compositions (Table 1).

(iii) Electrochemical Impedance Spectroscopy (EIS) studies

EIS was applied to give better information on electrochemical corrosion resistance performance and corrosion protection mechanism of nanocomposite coatings along with the role of TiO₂ and Ce-TiO₂ loading in PEUTES. The capacitive loop at high frequency is ascribed to the charge transfer resistance (R_{ct}) and diameter of the capacitive loop related to R_{ct} in the Nyquist plots representing the impedance of the samples.³⁹ Nanocomposite coatings show higher diameter and hence greater impedance value in Nyquist plots (Supplementary figure 6) than that of PEUTES coatings. The Nyquist plot of PEUTES (Supplementary figure 6a) shows phenomenon of diffusion in coatings, acquiring Warburg impedance shape, suggesting that the electrolyte penetrates into the polymeric matrix.⁴² Additionally, at higher frequencies, the surface of PEUTES exhibit charge transfer behavior, a sign of initiation of corrosion process.⁴⁰ Nanocomposite coatings show no charge transfer behavior and diffusion tail even after prolonged exposure to the electrolyte solution for 144 h (Supplementary figure 6b-c) with the exception to the PEUTES-Ce-TiO₂-II nanocomposite coatings due to the formation of redox couple Ce⁺³/Ce⁺⁴ (Supplementary figure 6d) as discussed in section 3.10 (i).⁹

Similar results were also obtained from Bode plots (Figure 11) where the impedance values for TiO₂ ($\approx 10^7 \Omega$), Ce-TiO₂-I ($\approx 10^8 \Omega$) and Ce-TiO₂-II ($\approx 10^6 \Omega$) dispersed nanocomposite coatings were 2-3 fold higher (Figure 11 a-d) as compared to that of plain PEUTES ($10^5 \Omega$) coatings. The lowest frequency impedance modulus $|Z|_{0.01\text{Hz}}$, used to estimate the extent of corrosion activity, was found to be stable in case of nanocomposite coatings, suggesting that the aggressive species could not diffuse and reach the metal surface.⁴²

The enhanced corrosion protective performance can be accredited to the presence of nanoparticles in interstitial spaces, which induced good locking effect as well as good barrier

property at coating metal interface. Besides, the enhanced hydrophobic nature of the nanocomposite coatings as evident from contact angle images (Figure 11) this can be one of the reasons for improved corrosion protective ability of composite coatings in the said medium. The high R_p values of nanocomposite coatings in comparison to PEUTES and bare CS, revealed that the nanocomposite coatings can effectively suppress the diffusion of corrosive electrolyte into the polymer matrix by forming a strong barrier at coating metal interface.

Literature revealed that the VO based polymer coatings do not show satisfactory performance under stringent corrosive environments.^{1,43} However it has been observed that the dispersion of metal oxide nano particles in such coating systems induces far superior corrosion protective and physicomechanical properties, which is also observed in present case that is the $\text{TiO}_2/\text{CeTiO}_2$ dispersed PEUTES systems have exhibited superior corrosion protective performance than those of earlier reported systems (Table 2).^{1,9,43,45,46} Further, no such work on TiO_2 and Ce-TiO_2 dispersed soy oil PEUTES coating has been reported till now. Although nano TiO_2 dispersed castor oil based polyurethane-esteramide and commercial polyurethanes coatings have been reported whose performance were found to be inferior to the present nanocomposite coatings. Among different compositions, PEUTES-Ce- TiO_2 -I shows best corrosion protection as no sign of degradation was observed at higher impedance value ($\approx 10^8 \Omega$) under lower frequency. The EIS results are well in agreement with that of PDP studies.

(iv) Salt mist test

Figure 12 shows the SEM micrograph of coated CS after 480 h of exposure to the salt mist test (in 5.0 wt. % NaCl of 90% humidity). Here also nanocomposite coatings (Figure 12 b) show no sign of degradation, only slight deposition of salt was observed on the coating surface, while in case of PEUTES (Figure 12 a) the formation of cracks and pin holes give rise to the corrosion. Hence, the salt mist test further confirms the better corrosion protection efficiency of nanocomposite coatings as compared to those of PEUTES and bare CS. The uniform, homogeneous dispersion of nanoparticles and dense hydrophobic network structure

of nanocomposite coatings protect the underlying metal substrate from the corrosive ions attack.

3.11. Corrosion mechanism

The PEUTES nanocomposite coatings provide protection to the CS metal substrate through the (i) electro-static interaction of polar group at coating-metal interface leading to the formation of well adhered and compact coating, (ii) the presence of silica, TiO₂ and Ce-TiO₂ nanoparticles in PEUTES act as strong barrier that inhibit the penetration of corrosive ion at the metal-coating interface, and (iii) the presence of these nanoparticles also induces locking effect at the interstitial spaces and healing the other coating artifacts (micro cracks and voids). Hence, the protection mechanism for PEUTES nanocomposite coatings (Figure 13) are governed by adhesion and locking effect of nanofillers, that provides barrier to the corrosion, and enhances the corrosion-protection efficiency of PEUTES nanocomposite coatings.

4. CONCLUSION

The TiO₂ and Ce doped (Ce-TiO₂) nanoparticles were synthesized in the green medium using castor oil via Sol-Gel technique. These nanoparticles were dispersed in soy polyesterurethane to prepare nanocomposite on CS surface. There physico-mechanical tests were performed by standard methods. Their anticorrosive performance of these coatings was tested in 3.5 wt % and 5 wt % NaCl solutions using PDP and EIS techniques and salt spray tests respectively. These studies revealed that the TiO₂ and Ce-TiO₂dispersed soy polyurethane green nanocomposite coatings have far superior physico-mechanical and corrosion resistance properties in comparison to other such reported systems. These coatings are expected to have a potential scope for their commercialization in the field of paints and coatings.

ASSOCIATED CONTENT

Supporting Information

Fatty acid extraction procedure, Equivalent electrical circuit, EDX spectra of nanoparticles, TEM micrographs of PEUTES and nanocomposites, ¹³C-NMR spectra of PEUTES, Optical micrographs for cross hatch test and Nyquist plot (Supplementary Figure 1-6) and Supplementary Table 1 physico-mechanical of PEUTES, PEUTES-TiO₂, PEUTES-Ce-TiO₂-I and PEUTES-Ce-TiO₂-II. The Supporting Information is available free of charge on the ACS Publications website.

AUTHOR INFORMATION

Corresponding Author

sharifahmad_jmi@yahoo.co.in, Tel no. +91 11 26827508, Fax: +91 11 26840229

Notes

The authors declare no competing financial interest.

ACKNOWLEDGEMENTS

One of the authors is thankful to CSIR, India (Obaid ur Rahman) for financial support in the form of CSIR senior research fellowship (vide grant No: 9/466 (0164) 2K13-EMR-I). The authors acknowledge the ‘Sophisticated Analytical Instrumentation Facility (SAIF)’ center, All India Institutes of Medical Sciences (AIIMS), New Delhi for TEM facility.

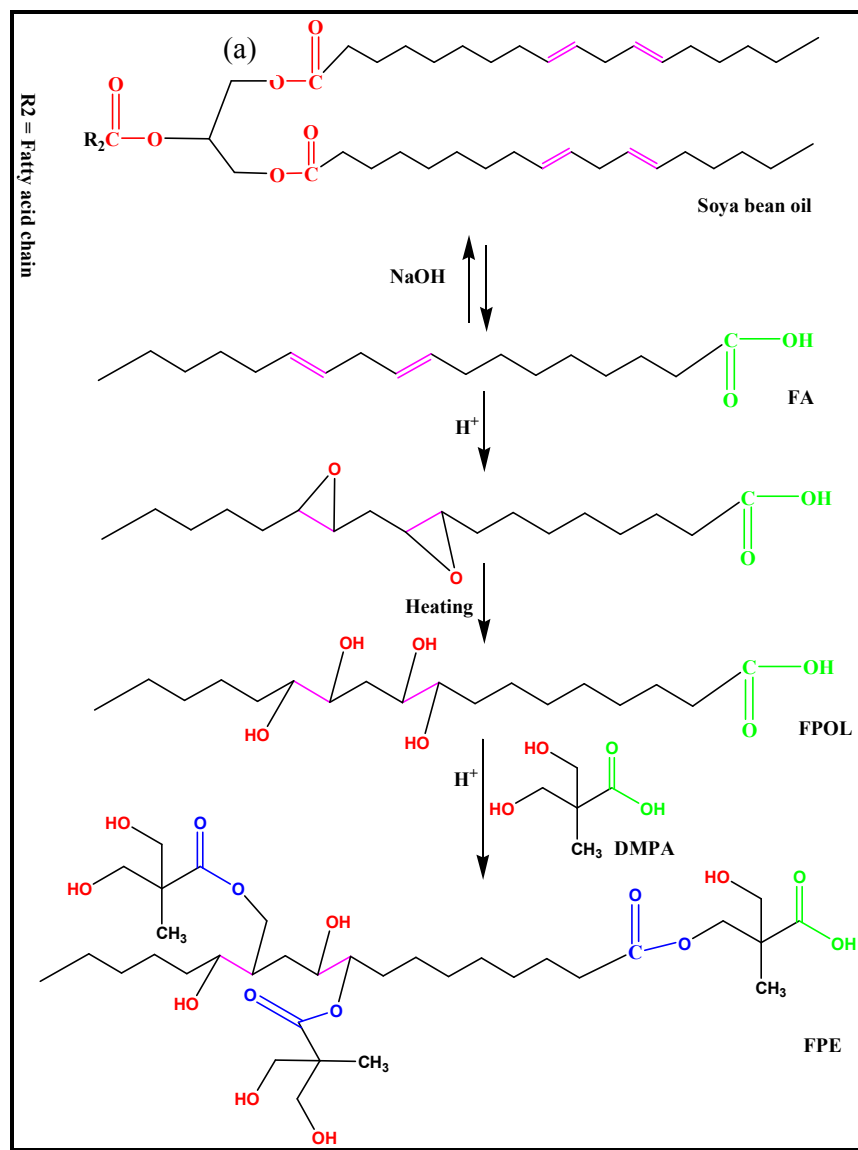
References

1. Guo, Z.; Wei, H.; Ding, D.; Wei, S., Anticorrosive Conductive Polyurethane Multiwalled Carbon Nanotubes NanoComposites. *J. Mater. Chem. A*. **2013**, *1*, 10805-10813.
2. Williams, J. C.; Starke Jr, E. A., Progress in structural materials for aerospace systems. *Acta Materialia*. **2003**, *51*, 5775-5799.
3. Pathan, S.; Ahmad, S., Synthesis, characterization and effect of s-triazine ring on physico-mechanical and electrochemical corrosion resistance properties of waterborne castor oil alkyd. *J. Mater. Chem. A*. **2013**, *1*, 14227-14238.
4. Deveci, H.; Ahmetli, G.; Ersoz, M.; Kurbanli, R., Modified polystyrenes: Corrosion, physicomechanical and thermal properties evaluation. *Prog. Org. Coat.* **2012**, *73*, 1-7.
5. Narine, S. S.; Kong, X., Vegetable oils in production of polymers and plastics. *Bailey's Industrial Oil and Fat Products*, John Wiley & Sons, Inc. **2005**.
6. Alam, M.; Akram, D.; Sharmin, E.; Zafar, F.; Ahmad, S., Vegetable oil based eco-friendly coating materials: A review article. *Arabian Journal of Chemistry*. **2013**, *7*, 469-479.
7. Díez-Pascual, A. M.; Díez-Vicente, A. L., ZnO-reinforced Poly (3-hydroxybutyrate-co-3-hydroxyvalerate) Bionanocomposites with Antimicrobial Function for Food Packaging. *ACS Appl. Mater. Interfaces*. **2014**, *6*, 9822-9834.
8. Sanchez, C.; Julian, B.; Belleville, P.; Popall, M., Applications of hybrid organic-inorganic nanocomposites, *J. Mater. Chem.* **2005**, *15*, 3559-3592.

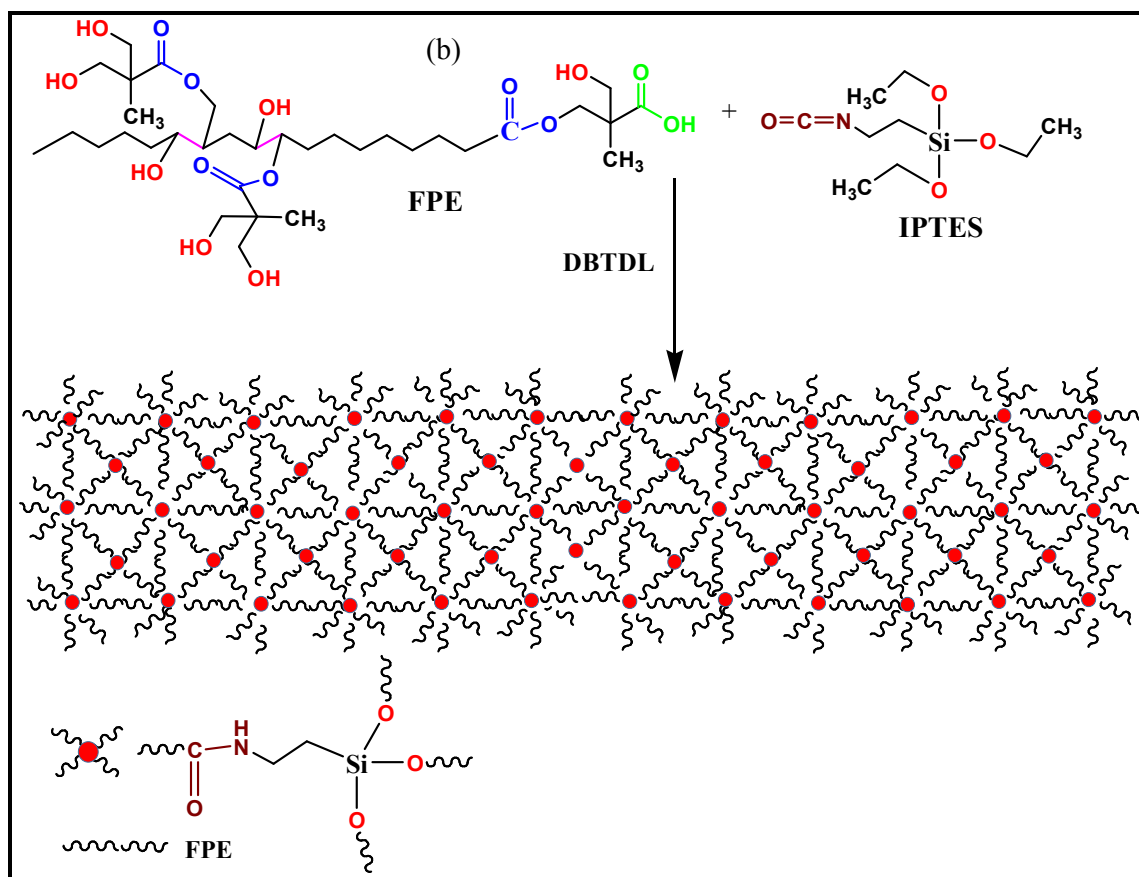
9. Li, S.; Wang, Q.; Chen, T.; Zhou, Z.; Wang, Y.; Fu, J., Study on cerium-doped nano-TiO₂ coatings for corrosion protection of 316 L stainless steel. *Nanoscale Res Lett.* **2012**, *7*, 1-9.
10. Viana, B. C.; Ferreira, O. P.; Souza Filho, A. G.; Rodrigues, C. M.; Moraes, S. G.; Mendes Filho, J.; Alves, O. L., Decorating titanate nanotubes with CeO₂ nanoparticles. *J. Phys. Chem. C.* **2009**, *113*, 20234-20239.
11. Haas, M. J.; Scott, K. M.; Marmer, W. N.; Foglia, T. A., In situ alkaline transesterification: an effective method for the production of fatty acid esters from vegetable oils. *J. Am. Oil Chem. Soc.* **2004**, *81*, 83-89.
12. Sharmin, E.; Ashraf, S.; Ahmad, S., Synthesis, characterization, antibacterial and corrosion protective properties of epoxies, epoxy-polyols and epoxy-polyurethane coatings from linseed and Pongamia glabra seed oils. *Int. J. Biological. Macromolecules.* **2007**, *40*, 407-422.
13. Malmström, E.; Johansson, M.; Hult, A., Hyperbranched aliphatic polyesters. *Macromolecules.* **1995**, *28*, 1698-1703.
14. dell'Erba, I. E.; Hoppe, C. E.; Williams, R. J., Synthesis and Properties of Organic-Inorganic Hybrid Materials Based on Glycerol. *Ind. Eng. Chem. Res.* **2012**, *51*, 7793-7799.
15. Sharmin, E.; Akram, D.; Zafar, F.; Ashraf, S. M.; Ahmad, S., Plant oil polyol based poly (ester urethane) metallohybrid coatings. *Prog. Org. Coat.* **2012**, *73*, 118-122.
16. Pathak, S.; Khanna, A.; Sinha, T., HMMM cured corrosion resistance waterborne ormosil coating for aluminum alloy. *Prog. Org. Coat.* **2007**, *60*, 211-218.
17. Yeh, T.-C.; Huang, T.-C.; Huang, H.-Y.; Huang, Y.-P.; Cai, Y.-T.; Lin, S.-T.; Wei, Y.; Yeh, J.-M., Electrochemical investigations on anticorrosive and electrochromic properties of electroactive polyurea. *Polym. Chem.* **2012**, *3*, 2209-2216.
18. Ghosal, A.; Shah, J.; Kotnala, R. K.; Ahmad, S., Facile green synthesis of Nickel nanostructures using natural polyol and morphology dependent dye adsorption properties. *J. Mater. Chem. A* **2013**, *1*, 12868-12878.
19. Gionco, C.; Paganini, M. C.; Agnoli, S.; Reeder, A. E.; Giamello, E., Structural and spectroscopic characterization of CeO₂-TiO₂ mixed oxides. *J. Mater. Chem. A* **2013**, *1*, 10918-10926.
20. Wang, Z.; Liu, Y.; Martin, D. J.; Wang, W.; Tang, J.; Huang, W., CuO x-TiO₂ junction: what is the active component for photocatalytic H₂ production? *Phys. Chem. Chem. Phys.* **2013**, *15*, 14956-14960.
21. Xie, J.; Jiang, D.; Chen, M.; Li, D.; Zhu, J.; Lü, X.; Yan, C., Preparation and characterization of monodisperse Ce-doped TiO₂ microspheres with visible light photocatalytic activity. *Colloids Surf A.* **2010**, *372*, 107-114.
22. Nagaveni, K.; Hegde, M.; Madras, G., Structure and Photocatalytic Activity of Ti_{1-x}M_xO_{2±δ} (M= W, V, Ce, Zr, Fe, and Cu) Synthesized by Solution Combustion Method. *J. Phys. Chem. B.* **2004**, *108*, 20204-20212.
23. Zhang, J.; Peng, W.; Chen, Z.; Chen, H.; Han, L., Effect of Cerium Doping in the TiO₂ Photoanode on the Electron Transport of Dye-Sensitized Solar Cells. *J. Phys. Chem. C.* **2012**, *116*, 19182-19190.
24. Nasir, M.; Zhang, J.; Chen, F.; Tian, B.; Bagwasi, S., Study of Synergistic Effect of Ce and S Co-Doping on the Enhancement of Visible Light Photocatalytic Activity of TiO₂. *J. Phys. Chem. C.* **2013**, *117*, 9520-9528.
25. Silva, S. S.; Ferreira, R. A. S.; Fu, L.; Carlos, L. D.; Mano, J. F.; Reis, R. L. and Rocha, J., Functional Nanostructured Chitosan-Siloxane Hybrids. *J. Mater. Chem.* **2005**, *15*, 3952-3961.
26. Kannan, A. G.; Choudhary N. R. and Dutta, N., Fluoro-Silsesquioxane-Urethane Hybrid For Thin Film Applications. *ACS. Appl. Mat. Sci.* **2009**, *1*, 336-347.
27. Choudhury, B.; Borah, B.; Choudhury, A., Extending photocatalytic activity of TiO₂ nanoparticles to visible region of illumination by doping of cerium. *J. Photochem. Photobiol.* **2012**, *88*, 257-264.
28. Toscano-Underwood, C.; West, J.; Fitt, B.; Todd, A.; Jedryczka, M., Development of phoma lesions on oilseed rape leaves inoculated with ascospores of A-group or B-group *Leptosphaeria maculans* (stem canker) at different temperatures and wetness durations. *Plant Pathology.* **2001**, *50*, 28-41.

29. Fauhl, C.; Reniero, F.; Guillou, C., ¹H NMR as a tool for the analysis of mixtures of virgin olive oil with oils of different botanical origin. *Magn. Reson. Chem.* **2000**, *38*, 436-443.
30. Bhunia, H.; Nando, G.; Chaki, T.; Basak, A.; Lenka, S.; Nayak, P., Synthesis and characterization of polymers from cashewnut shell liquid (CNSL), a renewable resource II. Synthesis of polyurethanes. *Eur. Polym. J.* **1999**, *35*, 1381-1391.
31. Siyanbola, T.; Sasidhar, K.; Anjaneyulu, B.; Kumar, K.; Rao, B.; Narayan, R.; Olaofe, O.; Akintayo, E.; Raju, K., Anti-microbial and anti-corrosive poly (ester amide urethane) siloxane modified ZnO hybrid coatings from *Thevetia peruviana* seed oil. *J.Mater. Sci.* **2013**, *48*, 8215-8227.
32. Kenawy, E.-R.; Worley, S.; Broughton, R., The chemistry and applications of antimicrobial polymers: a state-of-the-art review. *Biomacromolecules* **2007**, *8*, 1359-1384.
33. Trejo-Durán, M.; Martínez-Richa, A.; Vera-Graziano, R.; Alvarado-Méndez, E.; Castano, V., Structural and thermal characterization of hybrid materials based on TEOS and DCN. *J. Appl. Polym. Sci.* **2009**, *111*, 794-804.
34. Sun, C.; Lee, J. S.; Zhang, M., Magnetic nanoparticles in MR imaging and drug delivery. *Adv. Drug Delivery Rev.* **2008**, *60*, 1252-1265.
35. Chattopadhyay, D.; Webster, D. C., Thermal stability and flame retardancy of polyurethanes. *Prog. Polym. Sci.* **2009**, *34*, 1068-1133.
36. Erdmann, L.; Uhrich, K., Synthesis and degradation characteristics of salicylic acid-derived poly (anhydride-esters). *Biomaterials* **2000**, *21*, 1941-1946.
37. Zhang, C.; Xia, Y.; Chen, R.; Huh, S.; Johnston, P. A.; Kessler, M. R., Soy-castor oil based polyols prepared using a solvent-free and catalyst-free method and polyurethanes therefrom. *Green Chem.* **2013**, *15*, 1477-1484.
38. Pan, X.; Sengupta, P.; Webster, D. C., High biobased content epoxy-anhydride thermosets from epoxidized sucrose esters of fatty acids. *Biomacromolecules* **2011**, *12*, 2416-2428.
39. Liu, Q.; Chen, D.; Kang, Z., One-Step Electrodeposition Process To Fabricate Corrosion-Resistant Superhydrophobic Surface on Magnesium Alloy. *ACS Appl. Mater. Interfaces.* **2015**, *7*, 1859-1867.
40. Shi, X.; Nguyen, T. A.; Suo, Z.; Liu, Y.; Avci, R., Effect of nanoparticles on the anticorrosion and mechanical properties of epoxy coating. *Surf. Coat. Technol.* **2009**, *204*, 237-245.
41. Huang, T.-C.; Su, Y.-A.; Yeh, T.-C.; Huang, H.-Y.; Wu, C.-P.; Huang, K.-Y.; Chou, Y.-C.; Yeh, J.-M.; Wei, Y., Advanced anticorrosive coatings prepared from electroactive epoxy-SiO₂ hybrid nanocomposite materials. *Electrochim. Acta.* **2011**, *56*, 6142-6149.
42. Prasai, D.; Tuberquia, J. C.; Harl, R. R.; Jennings, G. K.; Bolotin, K. I., Graphene: corrosion-inhibiting coating. *ACS nano.* **2012**, *6*, 1102-1108.
43. Weng, C.-J.; Huang, J.-Y.; Huang, K.-Y.; Jhuo, Y.-S.; Tsai, M.-H.; Yeh, J.-M., Advanced anticorrosive coatings prepared from electroactive polyimide-TiO₂ hybrid nanocomposite materials. *Electrochim. Acta.* **2010**, *55*, 8430-8438.
44. ur Rahman, O.; Ahmad, S., Physico-mechanical and electrochemical behavior of soy alkyd/Fe₃O₄ nanocomposite coatings. *RSC Advances* **2014**, *4*, 14936-14947.
45. Shaik M. R.; Alam M.; and Alandis N. M., Development of Castor Oil Based Poly(urethane-esteramide)/TiO₂ Nanocomposites as Anticorrosive and Antimicrobial Coatings. *Journal of Nanomaterials.* **2015**, *2015*, 1-10.
46. Arun M.; Kantheti S.; Ranganathan R.G.; Narayan R.; Raju K. V. S. N.; Surface modification of TiO₂ nanoparticles with 1,3,5-triazine based silane coupling agent and its cumulative effect on the properties of polyurethane composite coating. *J. Polym. Res.* **2014**, *21*, 600-609.

Figures and Scheme:



Scheme 1 a. Reaction scheme for the synthesis of FPE



Scheme 1 b. Reaction scheme for the synthesis of PEUTES

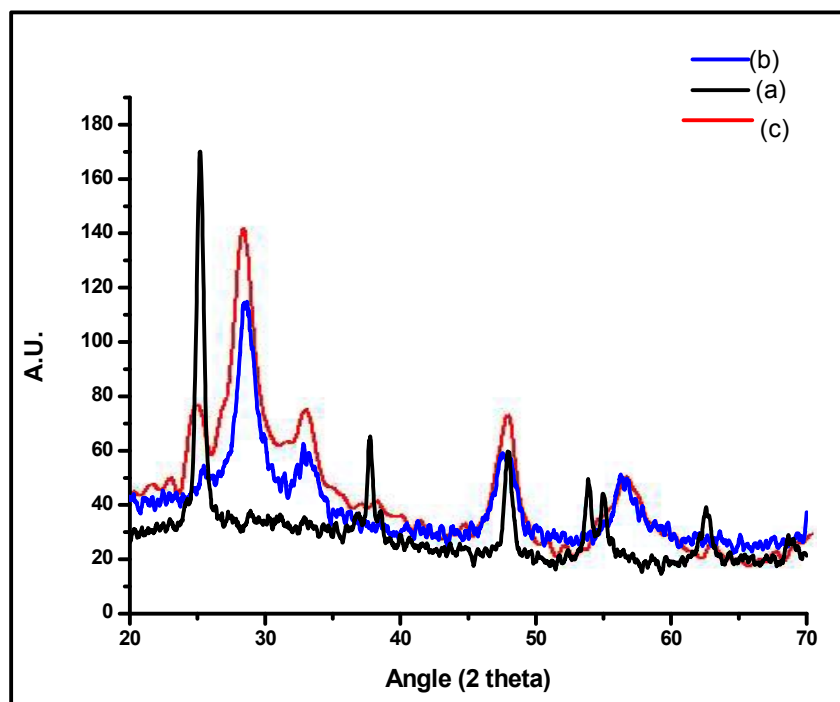


Figure 1 a. The XRD pattern of (a) TiO_2 nanoparticles JCPDS card no: (b) $\text{Ce-TiO}_2\text{-I}$ JCPDS card no: 49- 1606 nanoparticles (c) $\text{Ce-TiO}_2\text{-II}$ nanoparticles JCPDS card no: 49- 1606.

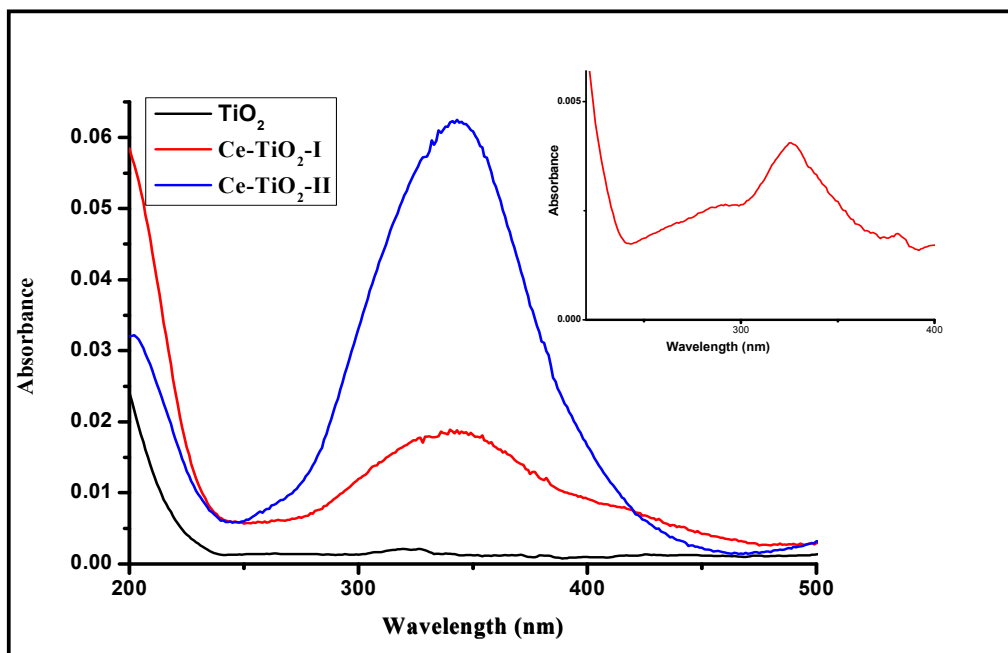


Figure 2. UV-Visible spectra of TiO_2 and Ce-TiO_2 nanoparticles

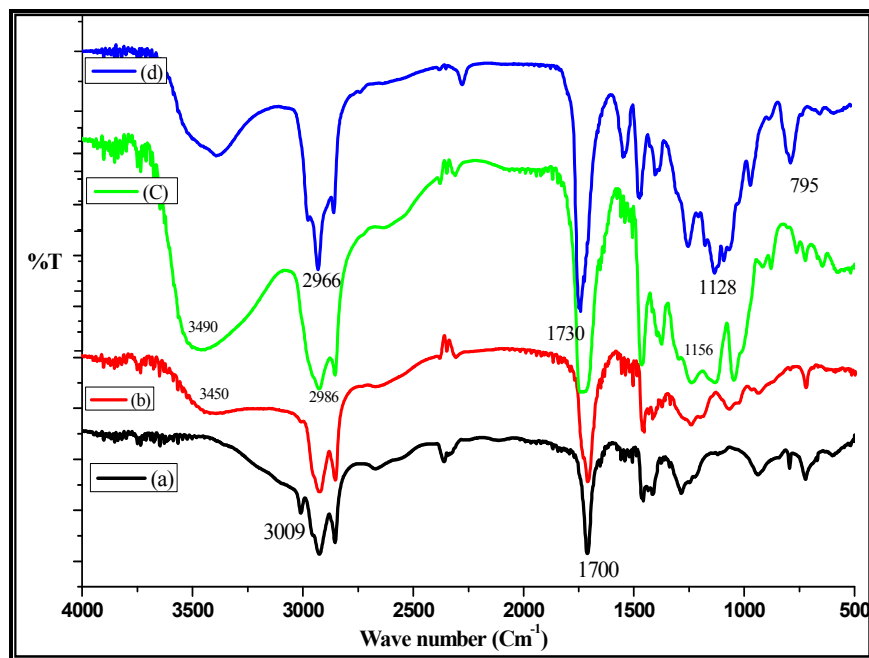


Figure 3. FT-IR spectra of (a) FA (b) FPOL (c) FPE and (d) PEUTES

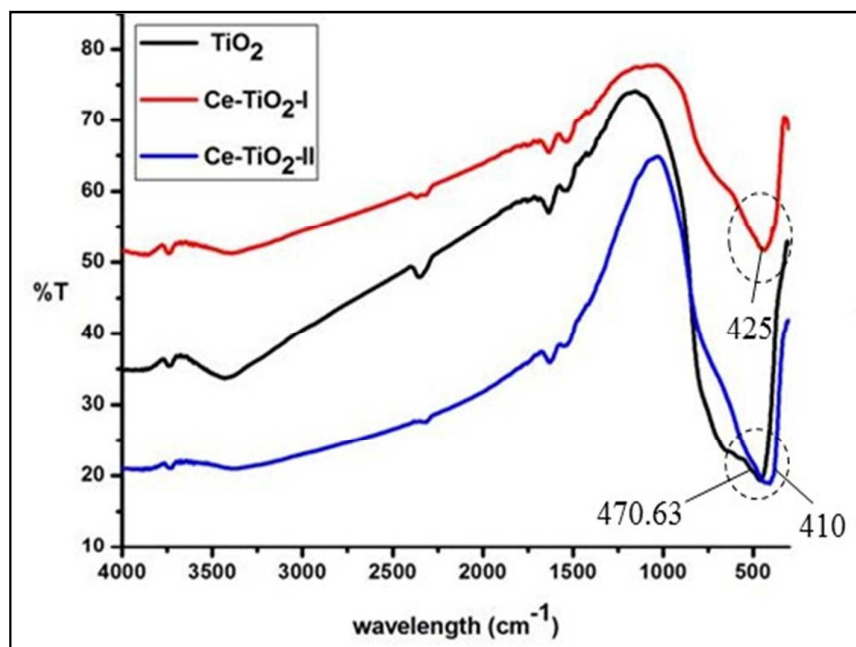


Figure 4. FT-IR spectra of TiO_2 , $\text{Ce-TiO}_2\text{-I}$ and $\text{Ce-TiO}_2\text{-II}$ samples

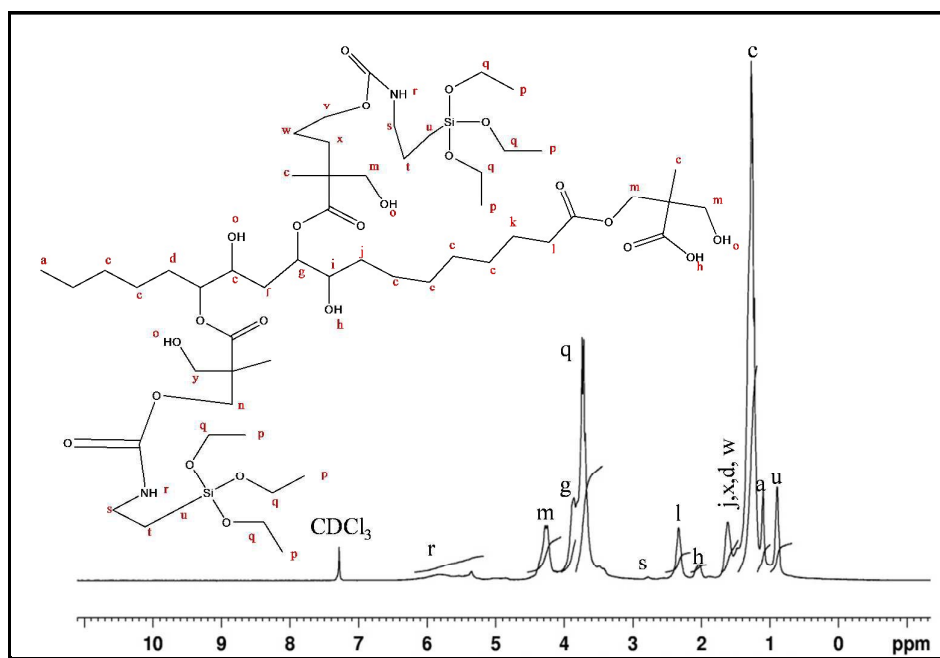


Figure 5. ¹H-NMR spectra of PEUTES

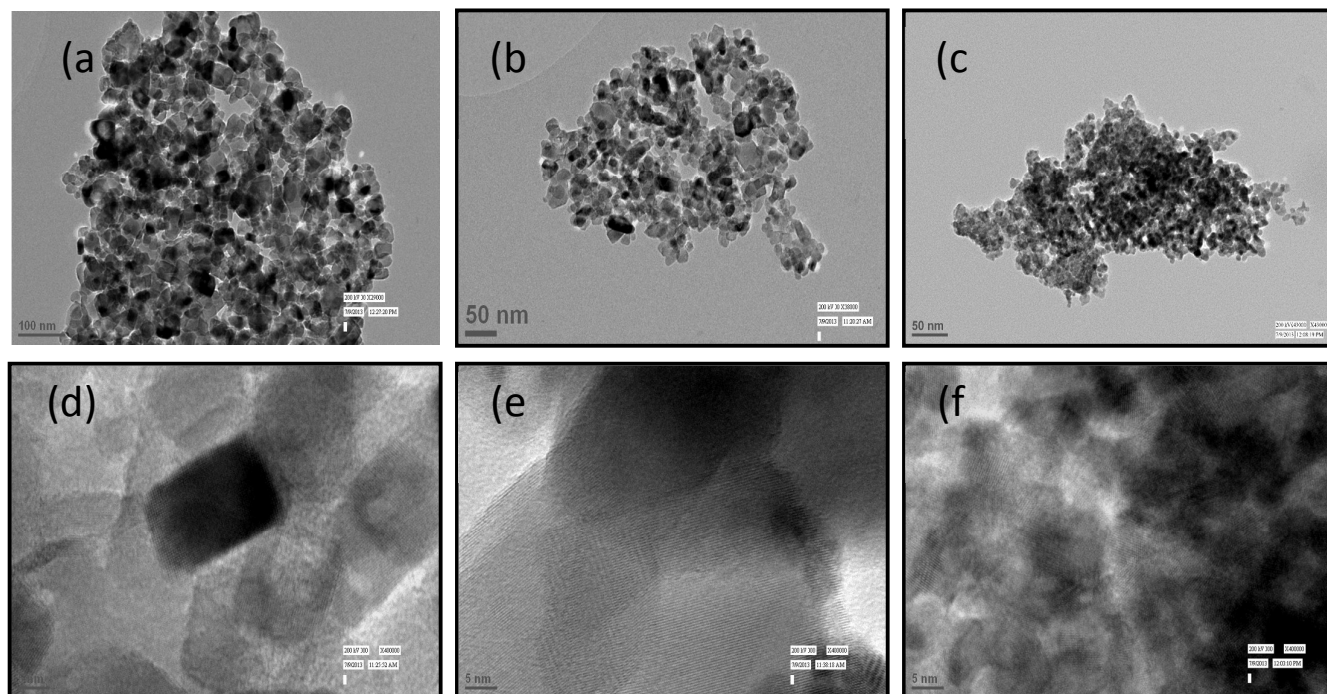


Figure 6. TEM micrographs of (a) TiO₂ nanoparticles (b) Ce-TiO₂-I nanoparticles (c) Ce-TiO₂-II nanoparticles (d) HR-TEM of TiO₂ nanoparticles (e) HR-TEM of Ce-TiO₂-I nanoparticles (f) HR-TEM of Ce-TiO₂-II nanoparticles.

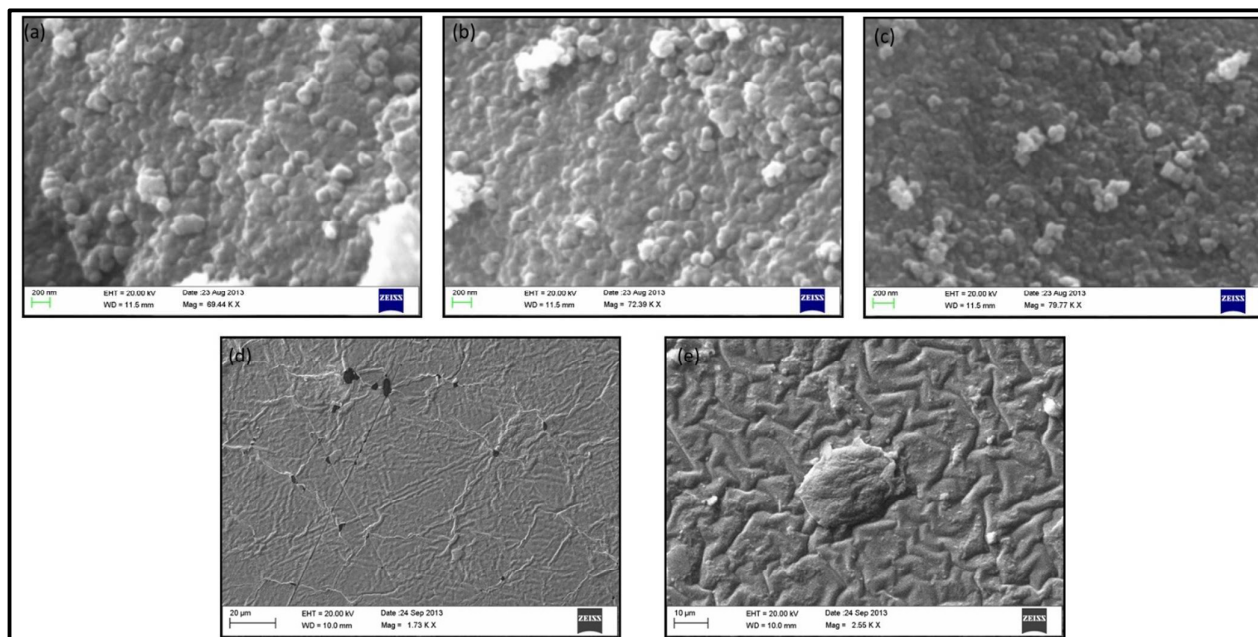


Figure 7 SEM micrograph of (a) TiO₂ nanoparticles (b) Ce-TiO₂-I nanoparticles (c) Ce-TiO₂-II nanoparticles (d) PEUTES at 1.73 KX (e) PEUTES at 2.55 KX.

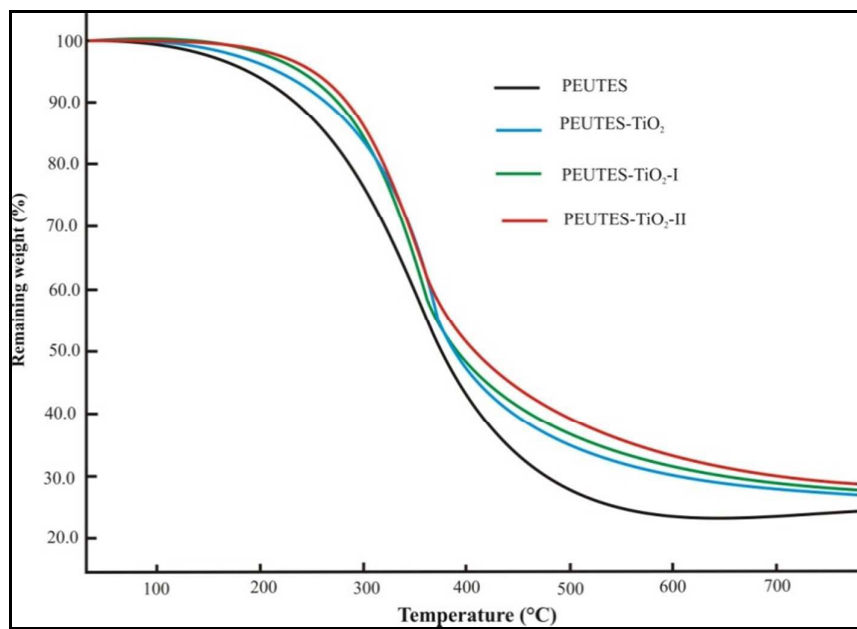


Figure 8. TGA thermograms of nanocomposite coatings

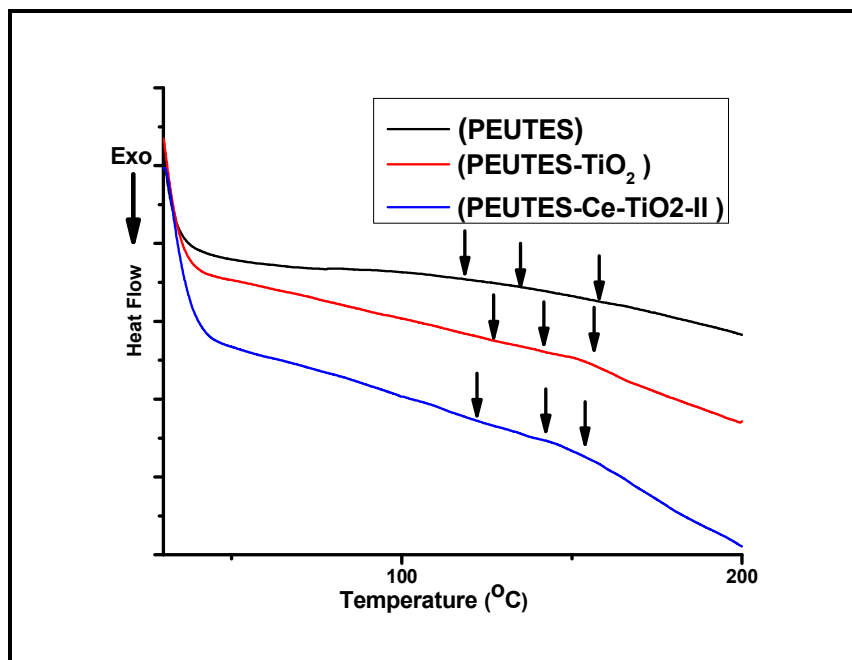


Figure 9. DSC thermograms of Nanocomposite coatings

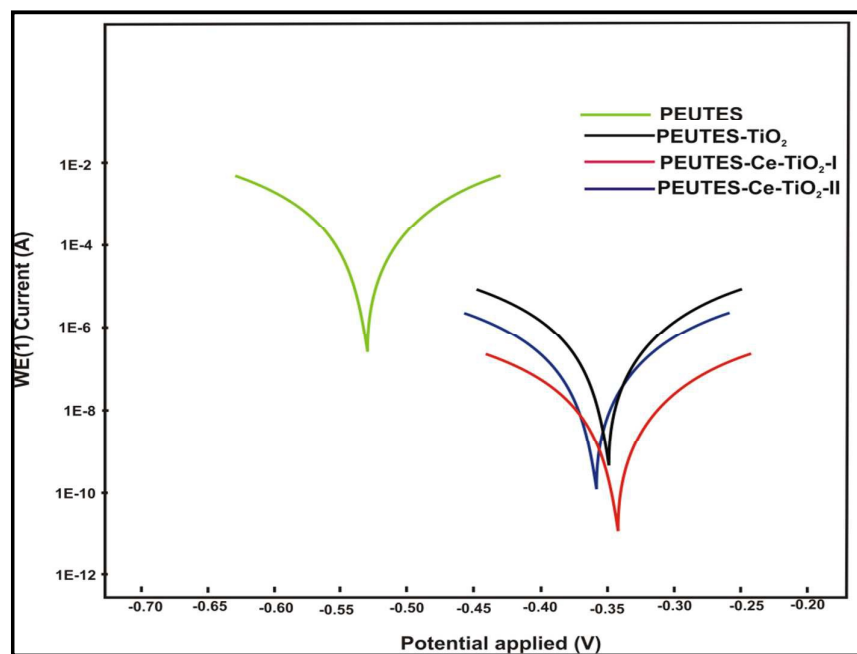


Figure 10. PDP curves of PEUTES, PEUTES-TiO₂ and different Composition of PEUTES-Ce-TiO₂

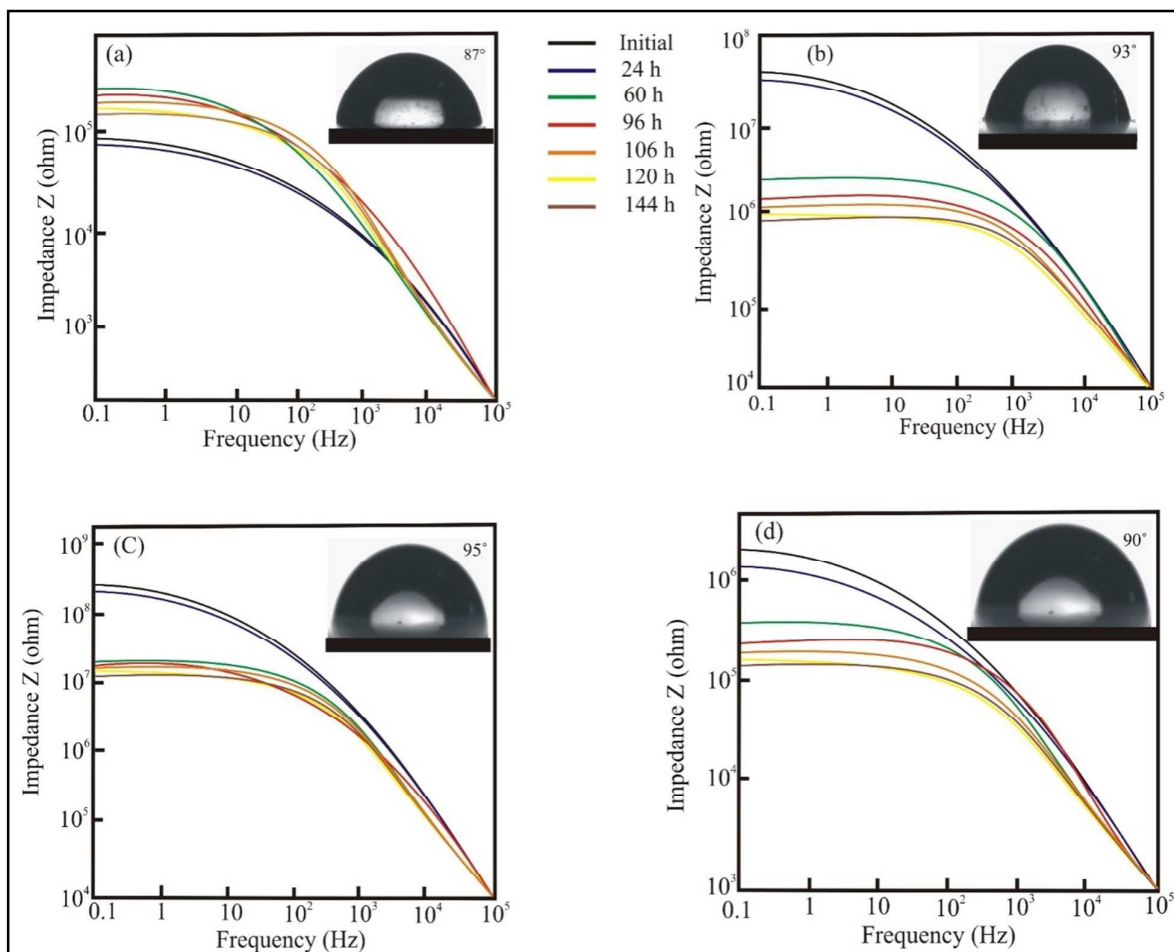


Figure 11. Bode plot in 3.5 wt % NaCl solution of PEUTES and nanocomposite coated samples (a) PEUTES(b) PEUTES-Ce-TiO₂ (c) PEUTES-Ce-TiO₂-I and (d) PEUTES-Ce-TiO₂-II

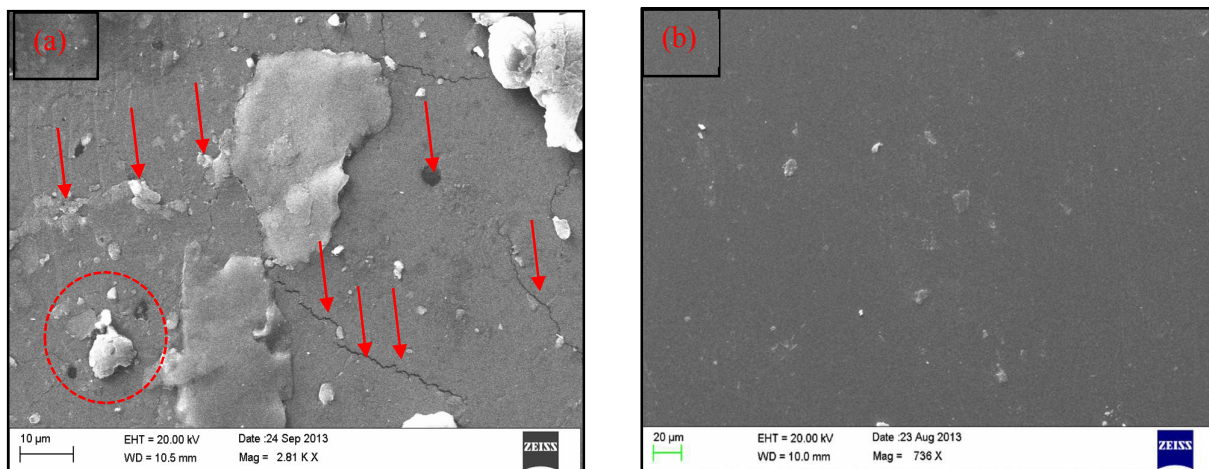


Figure 12. SEM micrograph after exposure to salt mist Chamber of (a) PEUTES (b) PEUTES-Ce-TiO₂-I.

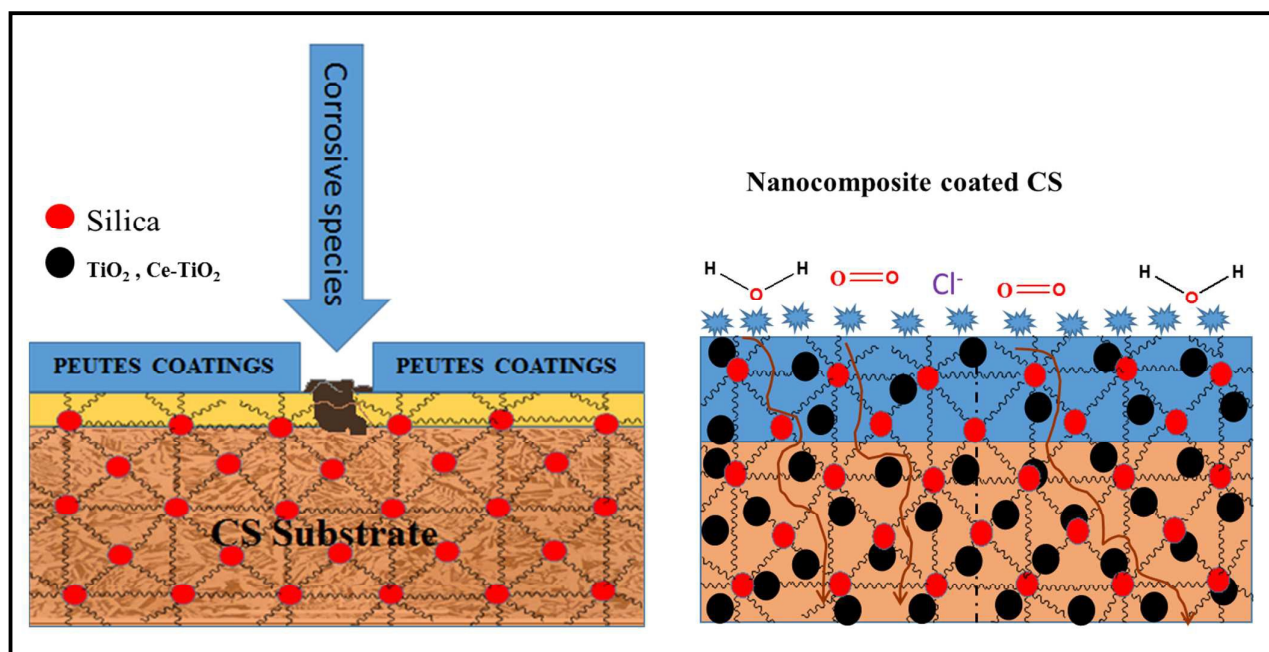


Figure 13. Mechanism of corrosion protection for PEUTES nanocomposite coatings

Table 1. PDP parameters of PEUTES, PEUTES-TiO₂ and different compositions of PEUTES-Ce-TiO₂ coated CS

Resin code	E _{corr} (V)	I _{corr} (A)	R _p (Ω)	Corrosion rate (mpy)
CS ⁴⁰	-0.66951	42.7	575.44	0.49615
PEUTES	-0.5327	4.970×10 ⁻⁶	13901	0.057752
PEUTES-TiO ₂	-0.3631	1.284×10 ⁻⁸	3.4251×10 ⁶	0.000149
PEUTES-Ce-TiO ₂ -I	-0.3337	6.757×10 ⁻¹⁰	3.7608×10 ⁷	7.8518×10 ⁻⁶
PEUTES-Ce-TiO ₂ -II	-0.3503	1.035×10 ⁻⁷	254590	0.001202

Table 2. Comparison of corrosion resistance properties of TiO₂ and Ce-TiO₂ polyester urethane hybrid nanocomposites coatings with other earlier reported systems in NaCl medium.

S.N	Coatings systems	I _{corr} (A)	Polarization resistance (R _p , Ω)	R _{pore} (Ω)	Impedance (R _{po} , Ω)	Reference
1	TiO ₂ and Ce-TiO ₂ soy oil polyester urethane hybrid nanocomposites coatings	6.76×10 ⁻¹⁰	3.7×10 ⁷	1.0×10 ⁷	1.0×10 ⁸	Present study
2	Castor Oil Based Poly(urethane-esteramide)/TiO ₂ nanocomposites coatings	8.27×10 ⁻⁷	--	--	--	41
3	cerium-doped nano-TiO ₂ metallic coatings	--	--	4.85×10 ⁴	4.58×10 ⁷	9a
4	TiO ₂ nanoparticles with 1,3,5-triazine based silane and polyurethane composite coating	2.4×10 ⁻¹⁰	4.7×10 ⁷	--	--	42
5	electroactive polyimide-TiO ₂ hybrid nanocomposite coatings	1.64×10 ⁻⁷	9460	0.439×10 ³	Less than 10 ⁷	39

For Table of Contents Only

Soy Polyester Urethane/TiO₂ and Ce-TiO₂ Nanocomposites Coatings: Preparation, Characterization and Evaluation of Electrochemical Corrosion Resistance Performance

Obaid ur Rahman and Sharif Ahmad*

Materials Research Laboratory, Department of Chemistry, Jamia Millia Islamia,
New Delhi-110025, India